



# Phase Transitions

A Multinational Journal

ISSN: 0141-1594 (Print) 1029-0338 (Online) Journal homepage: <http://www.tandfonline.com/loi/gpht20>

## A review on the mineral chemistry of the non-stoichiometric iron sulphide, $\text{Fe}_{1-x}\text{S}$ ( $0 \leq x \leq 0.125$ ): polymorphs, phase relations and transitions, electronic and magnetic structures

Haipeng Wang & Ian Salveson

To cite this article: Haipeng Wang & Ian Salveson (2005) A review on the mineral chemistry of the non-stoichiometric iron sulphide,  $\text{Fe}_{1-x}\text{S}$  ( $0 \leq x \leq 0.125$ ): polymorphs, phase relations and transitions, electronic and magnetic structures, Phase Transitions, 78:7-8, 547-567, DOI: [10.1080/01411590500185542](https://doi.org/10.1080/01411590500185542)

To link to this article: <https://doi.org/10.1080/01411590500185542>



Published online: 19 Aug 2006.



Submit your article to this journal [↗](#)



Article views: 451



View related articles [↗](#)



Citing articles: 65 View citing articles [↗](#)

## A review on the mineral chemistry of the non-stoichiometric iron sulphide, $\text{Fe}_{1-x}\text{S}$ ( $0 \leq x \leq 0.125$ ): polymorphs, phase relations and transitions, electronic and magnetic structures

HAIPIENG WANG\*<sup>†</sup> and IAN SALVESON<sup>‡</sup>

<sup>†</sup>School of Chemical Engineering, The University of Adelaide, SA 5005, Australia

<sup>‡</sup>Division of R&D, IDS Pty. Ltd, Adelaide, SA 5069, Australia

(Received 16 May 2005)

$\text{Fe}_{1-x}\text{S}$  ( $0 \leq x \leq 0.125$ ), the pyrrhotite group minerals are extremely complex in their chemical and physical properties, which largely attribute to the various non-stoichiometric compositions and myriad superstructures. In this article, a review is focused on the crystal structures, phase relations and transition of the pyrrhotite group minerals.

*Keywords:* Pyrrhotite; Iron sulphide; Phase diagram

### 1. Introduction

Pyrrhotite group is defined as all the iron monosulphides of the general formula  $\text{Fe}_{1-x}\text{S}$  ( $0 \leq x \leq 0.125$ ) that possesses the NiAs substructure, which has a hexagonal close-packed structure with  $[\text{FeS}_6]$  and  $[\text{SFe}_6]$  units [1, 2]. This includes troilite ( $\text{FeS}$ ) and monoclinic and hexagonal pyrrhotites. The pyrrhotites are extremely complex from both physical and chemical standpoints. They crystallize in the hexagonal or monoclinic system; troilite ( $\text{FeS}$ ) is hexagonal, whereas pyrrhotite ( $\text{Fe}_{1-x}\text{S}$ ) may be monoclinic or hexagonal. These minerals appear normally in massive form, commonly found in basic igneous or ultrabasic rocks, hydrothermal mineral deposits, and contact-metasomatic sediments. Interest in the pyrrhotite group arises from their occurrence in metallurgical process, their properties, and their common occurrence in ore deposits of many types. They are also of importance in terms of geomagnetism. They are all derivatives of the NiAs structure [3, 4]. Pyrrhotite minerals are abundant in nature, dark, brownish rusty colour on the surface. They are often in paragenesis with pyrite, chalcopyrite, pentlandite, and magnetite.

A better understanding of the chemical and physical behaviours of pyrrhotite are of commercial interest for mineral processing industry, as pyrrhotite is one of the major iron ores used as feedstock in flash smelting processes for metal extractions [5, 6]. Most pyrrhotite ores are ferrimagnetic in nature. Pyrrhotite can be separated

---

\*Corresponding author. Tel.: +81-8-83620302. Email: haipeng.wang@adelaide.edu.au

from its coexisting Ni-bearing ores by a combination of magnetic separation and flotation to obtain high-grade Ni concentrates. Apart from metallurgical usage pyrrhotite is also used for producing sulphuric acid. Recently, pyrrhotite was found to be of economical interest for wastewater treatment. It is used as a reducing agent to convert  $\text{Cr}^{\text{VI}}$  to  $\text{Cr}^{\text{III}}$ , which leads to Cr precipitates as  $\text{Cr}(\text{OH})_3$  [7].

## 2. Phases

### 2.1. Troilite

Troilite is a stoichiometric or near stoichiometric iron sulphide ( $\text{Fe}_{1-x}\text{S}$ ,  $x = 0-0.05$ ), having 2C superstructure of NiAs-type ( $a = \sqrt{3}A$ ,  $c = 2C$  where  $A$  and  $C$  are the axes of the NiAs subcell common to troilite and pyrrhotites), and  $P\bar{6}2c$  symmetry below  $140^\circ\text{C}$  [8–13]. It shows distortions from the ideal NiAs lattice positions (figure 1a and b); triangular groupings of iron atoms are displaced in the  $ab$ -plane forming contracted and dilated triangular units. The sulphur network is much less distorted with only a slight displacement of one-third of the sulphur atoms along the  $c$ -axis, away from the centre of Fe cluster [14]. The Fe cluster formed by three Fe atoms on  $ab$ -plane is shown in figure 1(b). Neighbouring Fe triangular clusters are positioned in two ways: stacked directly above one another along  $c$ -axis, and situated obliquely above one another (figure 1). Thus, a line connecting Fe atoms along  $c$ -axis is alternately parallel and inclined to  $c$ . The position of an iron cluster in the troilite cell is shown in figure 1(c). For troilite having ideal composition, FeS, the Fe–Fe distances in the same iron triangular cluster, directly above one another, and obliquely above one another are 2.925, 2.988, and 2.947 Å respectively [15].

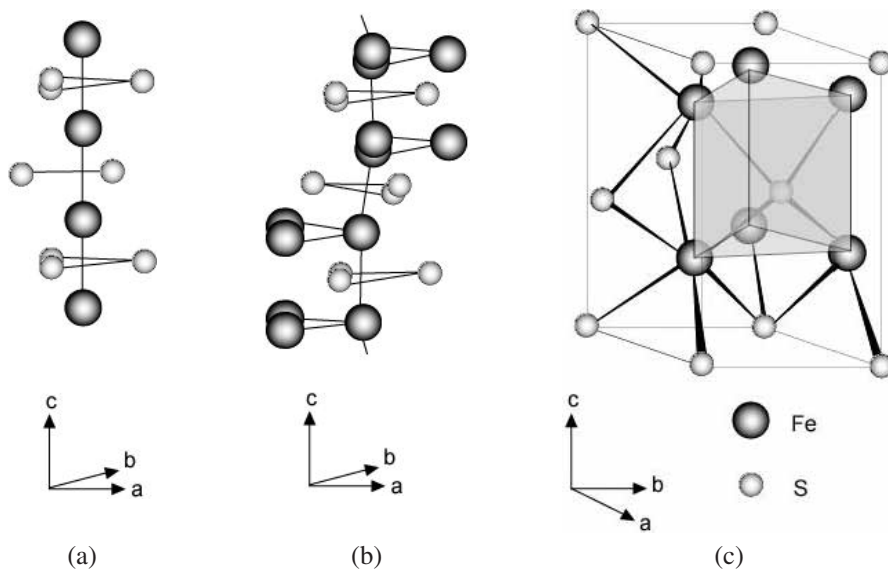


Figure 1. (a) Partial configuration of S and Fe atoms along  $c$ -axis in the NiAs substructure. (b) Partial atom configuration in troilite along  $c$  axis. Triangular Fe clusters are surrounded by distorted sulphur octahedra. (c) Fe clusters in the troilite cell, which is derived from the NiAs cell by doubling the  $c$ -axis, with  $a$ -axis deviating by  $30^\circ$  in  $ab$ -plane [15, 42].

The formation of Fe–Fe cluster is caused by Fe–Fe bonds formed by 3d electron overlapping when Fe–Fe distances below the critical value, 3.0 Å [15].

In nature, troilite is not as abundant as the more metal-deficient pyrrhotite minerals, and forms under strong reducing conditions [10]. One such occurrence is in swamps, where anaerobic bacteria can reduce sulphate to sulphide. Studies of swamp sediments show only low concentrations of troilite, but an abundance of fine crystalline pyrite [14]. Troilite is, however, found in most iron meteorites where it occurs in masses up to 5 cm in diameter. The magnetic moments on *ab*-planes are anti-ferromagnetically ordered at room temperature, and undergo a spin-flip transition ( $\alpha$ -transition) at 140°C [16–18], where the orientation of magnetic moments flips from  $\perp c$ -axis to  $\parallel c$ -axis [11, 19]. Magnetic moment disordering occurs at the Curie temperature, 315°C, at which anti-ferromagnetic FeS transforms to paramagnetic structure ( $\beta$ -transition) (figure 2).

The  $\beta$ -transition is accompanied by a phase transformation to the NiAs subcell (1C). The  $\beta$ -transition is a first-order transition (characterized by abrupt change in cell lattice). Although the conclusion that FeS undergoes magnetic structure variations during the  $\alpha$ -transition is widely accepted, there is dispute about whether a structural phase transition also occurs along with this magnetic transition [12, 20–33].

However, the majority of the research reports since the 1980s indicates FeS adopts the MnP-type structure between 140 and 315°C (between  $\alpha$ - and  $\beta$ -transition) [15, 34, 35]. The transition from the troilite (2C) to the MnP-type structure ( $\alpha$ -transition) is believed to be a second-order transition [11]. The MnP-type structure can be interpreted as a phase with subgroup symmetry of troilite. The similarity in the X-ray diffraction patterns of troilite and the MnP-type structure and the nature of continuous change in cell parameters (second-order transition) during the  $\alpha$ -transition may be the reason why the MnP-type structure was overlooked in earlier studies. Recently, the high temperature X-ray diffraction was used to distinguish these two similar phases [11]. It has been shown that the  $\alpha$ -transition

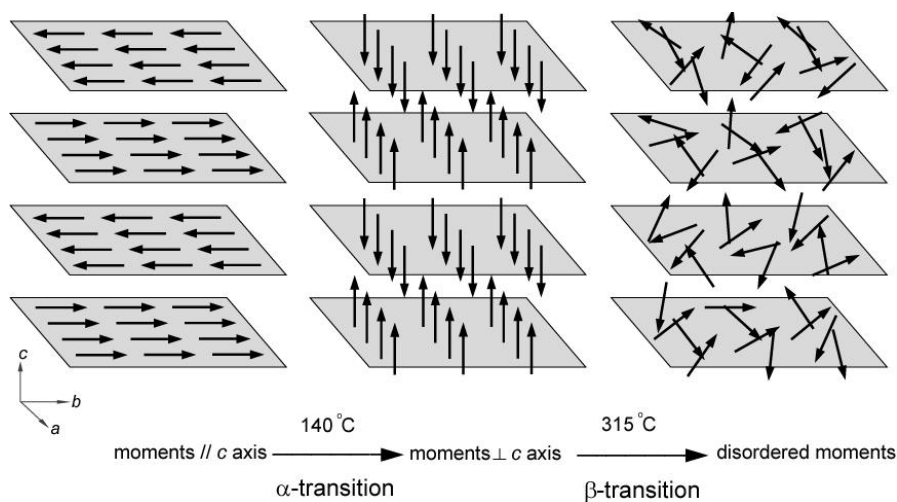


Figure 2. The transitions of magnetic moments configuration in FeS during a heating process ( $\alpha$ -transition at 140°C,  $\beta$ -transition at 315°C).

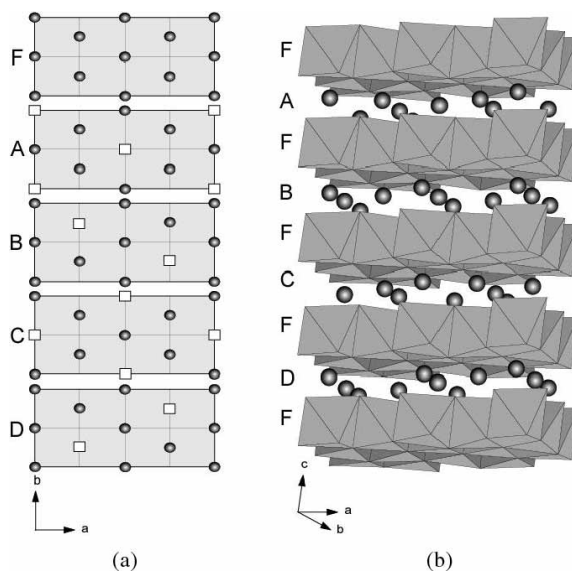


Figure 3. 4C monoclinic superstructure of pyrrhotite. (a) Four different vacancy arrangements in cation layer, A, B, C, and D. (b) Stacking sequence of vacancy layers and vacancy free layers [36, 37].

temperature is dependent on the starting stoichiometry of the troilite ( $\text{Fe}_{1-x}\text{S}$ ,  $x=0-0.05$ ). The larger the  $x$ , the lower the temperature of transition [11].

Metal-like iron states have been observed in troilite due to higher occupancy of Fe lattice sites compared to the more metal-deficient pyrrhotites, and increased Fe–Fe 3d orbital interactions within the constraints of the mineral structure.

## 2.2. Monoclinic pyrrhotite

Monoclinic pyrrhotite can be perceived as a derivative from FeS by subtraction of one-eighth iron atoms. The resultant structure contains alternating layers of full Fe sites and layers of Fe sites with vacancies, thereby lowering the symmetry from hexagonal to monoclinic [36, 37]. The 4C monoclinic structure may be regarded as the result of a slight distortion of the hexagonal structure [38], in which the  $c$  axis tilts with respect to the basal  $ab$ -plane [39]. The phase  $\text{Fe}_7\text{S}_8$  adopts a monoclinic structure in which vacancies are confined to every other site in alternate rows of sites within the vacancy layer. The vacancy layers are stacked in an ABCD sequence, quadrupling the unit cell along the stacking direction and leading to a superstructure of 4C. The various vacancy arrangements, A–D, are shown in figure 3(a).

The 4C superstructure of pyrrhotite can be expressed as  $(\dots \text{FAFBFCFDF} \dots)$ , where F represents a layer free of cation vacancies (figure 3b). Monoclinic pyrrhotite is not stable at high temperatures. Synthetic pyrrhotites, prepared using quenching techniques, are normally hexagonal even if the bulk composition is  $\text{Fe}_7\text{S}_8$ . Subsequent prolonged annealing at around  $200^\circ\text{C}$  is required to convert hexagonal  $\text{Fe}_7\text{S}_8$  to monoclinic  $\text{Fe}_7\text{S}_8$  [40].

In monoclinic pyrrhotite, and other pyrrhotites with distinct iron-deficient compositions, Fe atoms are octahedrally coordinated but S is both five- and

six-fold coordinated due to metal vacancies [41]. Due to the common sulphur deficiency nature of pyrrhotite, iron atoms exist in both states of  $\text{Fe}^{2+}$  and  $\text{Fe}^{3+}$  (hole state) [37]. The energetically most favourable magnetic configuration for pyrrhotite is that in which  $\text{Fe}^{3+}$  ions are confined to sites in vacancy bearing layers. The 4C pyrrhotite can be formulated as  $(\text{Fe}_2^{3+}\text{Fe}^{2+})(\text{Fe}_4^{2+})\text{S}_8$ . The electron transfer between  $\text{Fe}^{2+}$  and  $\text{Fe}^{3+}$  is very rapid, and Mössbauer spectroscopy cannot be used to detect the existence of Fe hole state ( $\text{Fe}^{3+}$ ) as the technique has a relatively long measurement time ( $10^{-8}$  s) compared to the creation and annihilation time of a hole state ( $10^{-14}$  s) [37, 42–44]. Thus, the presence of  $\text{Fe}^{3+}$  has not been confirmed by Mössbauer spectroscopy.

Monoclinic pyrrhotite shows strong ferrimagnetic behaviour. In fact, magnetic structures of all pyrrhotite group minerals are closely related to the ordering of iron atoms and vacancies in the vacancy bearing layers. The magnetic behaviour of monoclinic pyrrhotite is attributed to ferromagnetic alignment of cations within layers and anti-ferromagnetic coupling between adjacent layers [45]. The presence of vacancies in alternate layers results in an uncompensated moment, leading to ferrimagnetism [46].

Although monoclinic pyrrhotite is generally denoted as  $\text{Fe}_7\text{S}_8$ , it has a measurable composition range at room temperature [2, 47, 48]. There are two modifications of the  $\text{Fe}_7\text{S}_8$  phase, one with a slight monoclinic distortion and cell parameters (1A,  $2\sqrt{3}$ A, 4C). The second form can be described in terms of a trigonal supercell (2A, 3C) [41, 49, 50]. This phase is considered to be a metastable form at room temperature, as it normally exists in quenched samples, and has not been found in nature [50–52]. The stability field of 3C is shown in the MC zone of the phase diagram (see section 3). The 4C structure has been found only in natural pyrrhotite that has undergone cation and vacancy ordering processes over geological time [50, 53–55]. In other words, rapid cooling of  $\text{Fe}_7\text{S}_8$  from high temperature results in the formation of well-ordered 3C structure, whereas 4C structure is formed when the cooling rate is slow [56]. According to Nakazawa *et al.*, the 4C and 3C structures of  $\text{Fe}_7\text{S}_8$  differ not only in the arrangement of vacancies, but also in the type of Fe-clustering [55].

Li *et al.* [53] argued that upon heating 4C pyrrhotite ( $\text{Fe}_7\text{S}_8$ ) would undergo a series of structural adjustments from 4C to 3C (220°C) to NiAs-type structure (315°C). The magnetic structure of 4C comprises sheets parallel to the (001) plane of ferromagnetically aligned moments (intralayer) with anti-ferromagnetic coupling between neighbouring sheets (interlayer) along [001] direction.

The transformation of pyrrhotite with 3C superstructure to NiAs-type structure (1C) at higher temperature, 315°C, is also called  $\beta$ -transition, same as for troilite (see section 2.1).

The earlier-mentioned structural variations are accompanied by changes in the magnetic properties. The magnetic properties of pyrrhotite are altered as well, accompanied with the earlier structural variations. The ferrimagnetism of the monoclinic pyrrhotite due to magnetic moment ordering persists to 315°C, at which the magnetic moment of pyrrhotite drops drastically. This loss of ferrimagnetism is caused by long-range magnetic moment disordering or vacancy disordering at elevated temperatures [49]. This magnetic transition is accompanied by a major structural reorganization (3C–1C) [57]. The magnetic properties of pyrrhotite have been frequently measured through neutron diffraction experiments, as the magnetic moment is proportional to the magnetic reflection peak at

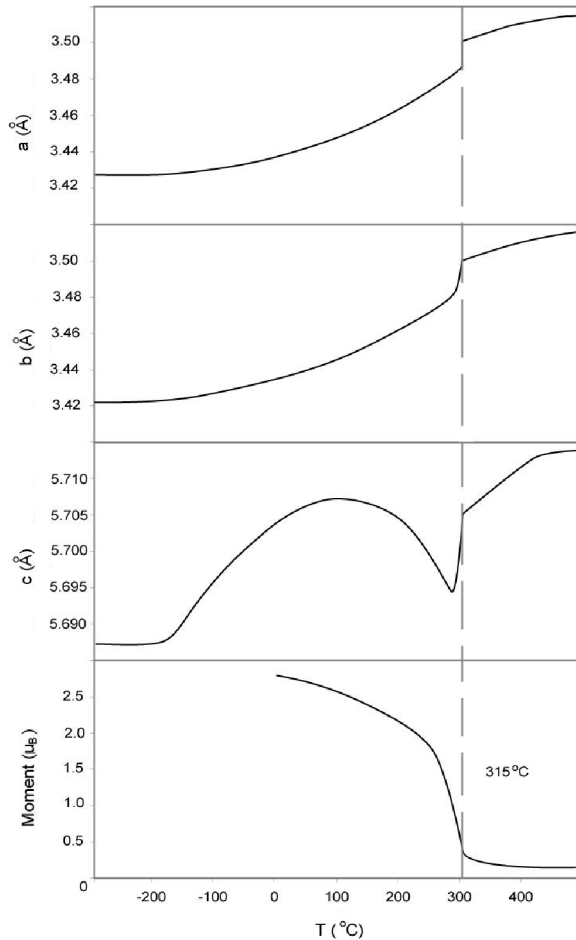


Figure 4. Changes in  $a$ ,  $b$ ,  $c$  parameters, and magnetic moment of monoclinic pyrrhotite with temperature [46].

$d \approx 5.7 \text{ \AA}$  ( $(001)_{\text{NiAs}}$ ) [58, 59]. The  $\beta$ -transition is a first-order transition, characterized by sudden changes in cell parameters or cell volume. The variations of cell parameters and magnetic moment of monoclinic pyrrhotite ( $\text{Fe}_7\text{S}_8$ ) with temperature are shown in figure 4 [46].

### 2.3. Hexagonal pyrrhotites

Similar to monoclinic pyrrhotites, vacancy bearing layers in hexagonal pyrrhotites determine the structural and magnetic properties of the various phases noted (from monoclinic 4C to hexagonal NC structures). Bertaut [60] noted a repulsion effect among vacancies in pyrrhotite. This observation was further developed by Powell [61] into the Vacancy Avoidance theory, which has been used to study the superstructures of pyrrhotite [61]. At high temperatures, the vacancy distribution is random and the unit cell of pyrrhotite is NiAs subcell, the 1C structure [62]. When the temperature decreases, the vacancies start to order and superstructures of NiAs subcell form [63]. Below  $300^\circ\text{C}$ , the diffusion of vacancies is effectively inhibited, and high-temperature structures are locked in metastable statuses [61, 64–66].

Many natural hexagonal pyrrhotites have been formed during a quenching process. The superstructures of NiAs subcell, except for 4C (see section 2.2) and 2C (see section 2.1), contain non-integral X-ray reflections attributed to the intergrowth of differently ordered domains [67]. Formation of superstructures does not appear to affect the short-range atom configurations, although detailed structural refinements of many superstructures are yet to be undertaken. Many of the hexagonal superstructures have very close stoichiometries but they appear to behave as separate phases (or polytypes) and were normally treated as such when delineating phase diagrams. Nakazawa and Morimoto [68, 69] sorted the numerous superstructures into five categories according to their multiplicities of the NiAs sublattice. The five categories of the superstructures are: (1) 2C for troilite, (2) 4C for monoclinic pyrrhotite, (3) *NC* ( $a = 2A$ ;  $c = NC$ ,  $N$  varies continuously between 5.0 and 11.0 [68–71]), (4) *MC* ( $a = 2A$ ;  $c = MC$ ,  $M$  varies between 3.0 and 4.0), (5) *NA* ( $a = NA$ ;  $c = 3C$ ,  $N$  varies continuously between 40 and 90). Note  $A$  and  $C$  are respectively the  $a$  and  $c$  parameters of NiAs subcell. The most well-studied superstructures in nature, 5C ( $\text{Fe}_9\text{S}_{10}$ ), 6C ( $\text{Fe}_{11}\text{S}_{12}$ ), and 11C ( $\text{Fe}_{10}\text{S}_{11}$ ), belong to the *NC* category [70, 71]. Although 5C, 6C, and 11C are crystallographically distinguishable, they are treated as one phase, *NC*, in the studies of phase relations. This is because they act as a single phase during phase transitions, and that their compositions fall into a very narrow range (47.37–47.83 at.% of Fe) [68–71]. These superstructures are best described in terms of stacking of fully occupied and ordered defective iron layers normal to the  $c$ -axis. Each structure is characterized by a regular succession of such layers, corresponding to an integral supercell multiplicity  $N$ , where  $c = NC$ . The multiplicity  $N$  is related to the general chemical formula  $\text{Fe}_{m-1}\text{S}_m$  ( $m > 8$ ) by  $N = 0.5m$  (when  $m$  has an even value), or  $N = m$  (when  $m$  has an odd value) [71]. This formulism only serves for the convenience of describing the superstructures in pyrrhotite. In fact, pyrrhotites with non-integral multiplicity superstructure are more common, as the  $m$  (as in  $\text{Fe}_{m-1}\text{S}_m$ ) is not necessarily an integer and changes continuously with composition and temperature [71]. Stacking disorder between filled and vacancy bearing layers gives rise to non-integral  $N$  values, and thus to an apparently incommensurate  $c$ -axis repeat [72–74]. These pyrrhotites are often referred to just as hexagonal pyrrhotite, and have compositions in the region between troilite and monoclinic pyrrhotite. These superstructures can either be expressed as  $\text{Fe}_9\text{S}_{10}$ ,  $\text{Fe}_{10}\text{S}_{11}$ ,  $\text{Fe}_{11}\text{S}_{12}$  or as a mixture of the stoichiometric phases with troilite or with monoclinic pyrrhotite [36, 68, 75–77].

The hexagonal pyrrhotites can be distinguished from the monoclinic phase by means of chromic acid etching [78] or by using magnetic colloid solution [79] under reflected light microscopy on polished samples. The chromic acid etching method is said to be difficult to apply to synthetic samples due to the fine exsolution texture and small grain size, but magnetic colloids in conjunction with X-ray identifications apparently work well on synthetic samples, as the magnetic colloid attracts to ferromagnetic areas [8].

#### 2.4. “Anomalous” monoclinic pyrrhotite

Clark [47] described a pyrrhotite with 46.4 at.% Fe in which the intensity of the ( $4\bar{0}8$ ) X-ray diffraction peak is greater than that of (408), the reverse of the normal situation for monoclinic pyrrhotite. This “anomalous” pyrrhotite, as it was denoted, appears to be widespread in the low-temperature and sedimentary environments [47].

It can be distinguished from normal monoclinic pyrrhotite by its weaker ferrimagnetism (or even anti-ferromagnetism). The “anomalous” monoclinic pyrrhotite unlike normal monoclinic pyrrhotite, which is a primary mineral, is secondary in origin [80–82]. In nature, pyrrhotite can exist in an environment open to oxygen. Thus, the composition of a primary pyrrhotite can be altered to a more metal-deficient secondary pyrrhotite by partial oxidation of iron. This process converts a hexagonal pyrrhotite to the secondary monoclinic pyrrhotite, even though this alteration could be difficult to distinguish from the oxidation of pyrrhotite by oxygen. The formation of “anomalous” monoclinic pyrrhotite through oxidation process has been discussed by Taylor [80], Kübler [81], Genkin [82], and Desborough and Carpenter [21]. The stability field of this “anomalous” secondary pyrrhotite, to our best knowledge, has not been ascertained.

### 3. Phase diagram

The phase relations in FeS–FeS<sub>2</sub> system have been the subjects of numerous investigations [8, 33, 41, 72, 83–85]. There is general agreement between a large number of studies on the phase relations at higher temperatures (>350°C), but much contradictory evidence at lower temperature ranges (<350°C). It is a daunting task to determine a solvus between the various pyrrhotite polymorphs due to the similarity of their powder diffraction patterns, as they form a series of chemically and structurally supercell phases [67]. At low temperatures, these pyrrhotite supercell phases might form metastable phase assemblages, which will seriously affect the accuracy of the determination of an equilibrium solvus. Some difficulties also occurred for the determination of phase solvus at high temperatures, as some high-temperature phases cannot be quenched for room-temperature measurement. The preservation of high-temperature crystal structures with pyrrhotite phases becomes problematic when  $T > 308^\circ\text{C}$  [39, 68, 86]. For sulphur-rich samples, the pyrrhotite compositions will invariably transect its equilibrium solvus, and produce large deviation from equilibrium compositions. In other words, for some pyrrhotite compositions ranges, no matter how fast the pyrrhotite samples are quenched from high temperature ( $T > 308^\circ\text{C}$ ) to room temperature, an oversaturation-induced phase exsolution might more or less affect the preservation of the high-temperature phase structure and composition. This problem has been successfully overcome by using high-temperature single crystal (or powder) X-ray diffraction methods [8, 69, 87].

Kissin and Scott [8] systematically investigated the low-temperature phase diagram near the most metal-deficient compositions using a hydrothermal recrystallization method. This method largely overcomes the problem of the long annealing requirement to achieve reaction equilibrium by dry synthesis experiment [88–91]. It gives more trustworthy results for phase relations. Their data and earlier reports on the pyrrhotite phase relations were summarized to give a relatively accurate and complete phase relations for low temperatures [8]. Combining the high-temperature phase diagram, figure 5 gives the complete FeS–FeS<sub>2</sub> phase relations covering the temperature range 25–1200°C.

The solvus between 1C pyrrhotite and pyrite continues below 750°C along the slope proposed by Toulmin and Barton [90] and Arnold [83] to 315°C, where the 1C phase starts to transform into *MC* superstructure ( $M = 3.0\text{--}3.3$ ). This temperature

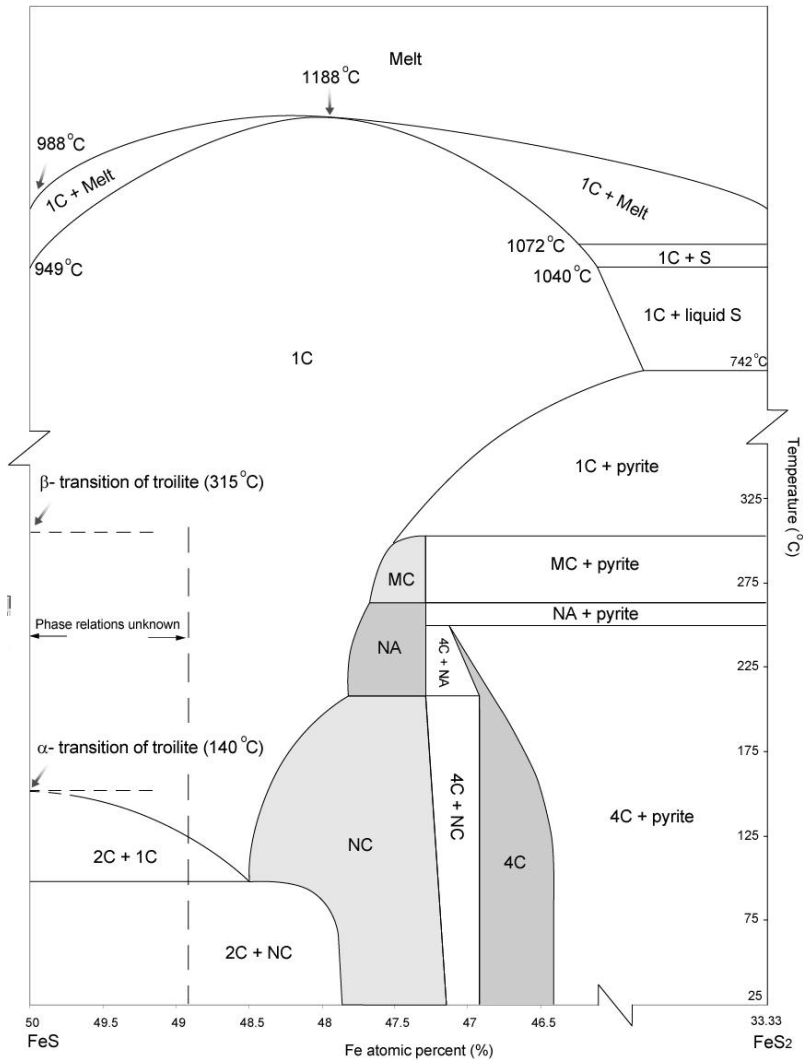


Figure 5. FeS–FeS<sub>2</sub> phase diagram [8, 33, 41, 72, 83–85].

coincides with the  $\beta$ -transition temperature. The solvus then proceeds along a similar slope down to 262°C, with the exsolution of *NA* superstructure. In the narrow temperature range from 262 to 254°C, *NA* pyrrhotite coexists with pyrite if the initial bulk composition contains less than 47.5 at.% Fe. The stability field of monoclinic pyrrhotite near 254°C is very narrow and many earlier researchers considered it restricted to Fe<sub>7</sub>S<sub>8</sub> (46.67 at.% Fe) [39, 47, 92–94], but it has been found that the monoclinic pyrrhotite is able to exist over a wider composition range at lower temperatures (e.g. 46.4–46.9 at.% Fe at 115°C [8]). Below 209°C, *NA* pyrrhotite will be transformed into *NC* structure [16–68, 70], and its stable composition field becomes wider with increasing temperature until around 90–100°C, a eutectic temperature, where three phases coexist (1C + 2C + *NC*) [95–97]. Below the eutectic temperature, 2C superstructure (troilite) coexist with *NC* pyrrhotite,

of composition 47.8 at.% Fe at room temperature [33]. Viewed under a crossed polars microscope, the images of the 2C and NC phases under go extinction simultaneously, indicating that the *c*-axes of these two phases lie in parallel in the intergrowth [2]. The temperature at which pyrite melts incongruently (742°C) is from Kullerud and Yoder [98].

Arnold [83] proposed an idea of “Pyrrhotite Geothermometer”, which utilizes the temperature dependence of the composition of pyrrhotite coexisting with pyrite in a sulphide ore. The fundamental assumption of this pyrrhotite geothermometer was that a unique composition of hexagonal pyrrhotite coexists with pyrite along the pyrrhotite–pyrite solvus (figure 5) [8]. However, the geothermometer is only valid for low temperatures ( $T < 314^\circ\text{C}$ ), as pyrrhotite–pyrite ores at higher temperatures are unquenchable [8]. Pyrrhotite solvus exhibits a strong tendency to re-equilibrate with decreasing temperature.

Li and Franzen [49] stated that composition of troilite can vary in a narrow range (FeS to  $\text{Fe}_{0.95}\text{S}$ ). The phase transitions for stoichiometric troilite (FeS) have been well studied (troilite–MnP-type ( $140^\circ\text{C}$ )–1C pyrrhotite ( $315^\circ\text{C}$ )). However, the phase transitions studies for non-stoichiometric troilite (say  $\text{Fe}_{0.95}\text{S}$ ) have only been conducted for  $\alpha$ -transition (troilite–MnP-type) [97, 99, 100]. In these earlier studies for  $\alpha$ -transition solvus, the MnP-type phase was treated as 1C pyrrhotite, which has been proven imprecise. Figure 5 does not include the  $\beta$ -transition curves for the range of 49.0–50.0 at.% Fe, as there is no statistical result on  $\beta$ -transition solvus extending to the troilite composition  $\text{Fe}_{0.95}\text{S} \sim \text{FeS}$ .

The trigonal pyrrhotites (3C, see section 2.2), here denoted as *MC* instead of 3C, as in nature, normally exhibit a multiplicity (*M*) slightly larger than 3 ( $3 < M < 4$ ). Thus, it is more accurate to use *MC* in the phase diagram.

The phase diagram also gives guidance for the estimation of coexisting phases in an assemblage. At low temperatures, with the increase in iron content in bulk pyrrhotite compositions, the possible assemblage shifts from (4C + NC) to (2C + NC) [70, 101–105] (figure 5).

## 4. Electronic structure

### 4.1. Orbital separation energy ( $\Delta$ ) and spin-pairing energy ( $P$ )

In pyrrhotite iron atoms are octahedrally coordinated with six sulphur atoms. The two Fe 3d  $e_g$  orbitals have higher energy than three Fe 3d  $t_{2g}$  orbitals, as  $e_g$  orbitals are directly repelled by sulphur atoms along *x*, *y*, *z* axes. The energy difference between three degenerate  $t_{2g}$  orbitals and two degenerate  $e_g$  orbitals is the orbital separation energy ( $\Delta$ ). Spin-pairing energy ( $P$ ) is the energy barrier that an electron has to overcome in order to occupy the same orbital with another electron, forming an electron pair. For paired electrons, one is normally expressed as major spin ( $\alpha$ ), and the other minor spin ( $\beta$ ). The energy level of a minor spin electron is higher than that of a major spin electron by the amount of spin-pairing energy ( $P$ ). For an electron configuration with half filled  $t_{2g}$  orbitals, to add another electron means the additional electron will either occupy an empty higher energy level ( $e_g$  orbitals) or form an electron couple with an existing  $t_{2g}$  electron (electron pairing). The allocation of this additional electron depends on which energy barrier ( $\Delta$  or  $P$ ) is the lowest [106–112]. Nesbitt *et al.* [3] precisely determined the  $\Delta$  value of 1.5 eV, and  $P$  value of 2.25 eV, using synchrotron excited X-ray photoelectron spectra (SXPS).

The fact that  $P > \Delta$  in pristine pyrrhotite determines that the Fe atoms have a high-spin electron configuration.

#### 4.2. Energy level diagram

Fe 3d  $e_g$  orbitals ( $d_{z^2}$  and  $d_{x^2-y^2}$ ) in pyrrhotite direct towards the apical sulphur ligands, and each  $e_g$  orbital lobe is mixed with sulphur orbitals to produce strong bonding,  $\sigma$ , and anti-bonding,  $\sigma^*$ . However, the lobes of Fe 3d  $t_{2g}$  orbitals do not overlap with sulphur orbitals, but spread between  $x$ ,  $y$ , and  $z$  axes. The energy-level diagram of pyrrhotite is derived from the calculation by Nesbitt *et al.* [3], Tossell [43], and Sakkopoulos *et al.* [113] for  $[\text{FeS}_6]$  octahedral cluster with Fe–S distance equal to 2.5 Å, the average metal–sulphur separation in pyrrhotite. As shown in figure 5, the  $2a_{1g}$ ,  $2t_{1u}$  and  $1t_{2u}$  are Fe–S bonding orbitals, and  $2e_g$ ,  $1t_{2g}$ ,  $3t_{1u}$  and  $1t_{1g}$  are the non-bonding orbitals of sulphur (S 3p in character). According to the calculation of Tossell [43], 0.6 eV above  $1t_{1g}$  lies  $t_{2g}(\alpha)$  level, which has 80% Fe in character. The  $e_g(\alpha)$  level (60% Fe in character) lies 1.5 eV (the value of orbital separation energy,  $\Delta$ ) above  $t_{2g}(\alpha)$  [3]. The  $e_g(\alpha)$  is an anti-bonding level as is shown in figure 6, and that its energy level is higher than the former degenerated Fe 3d orbitals.

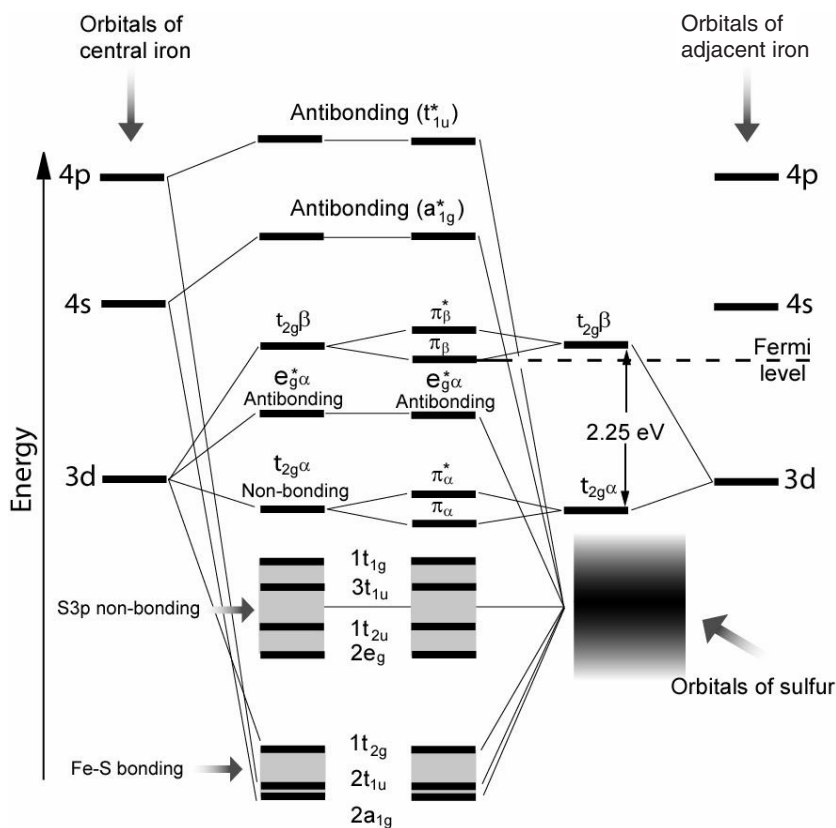


Figure 6. Pyrrhotite valence band structure based on molecular orbital (MO) theory [3, 47, 113].

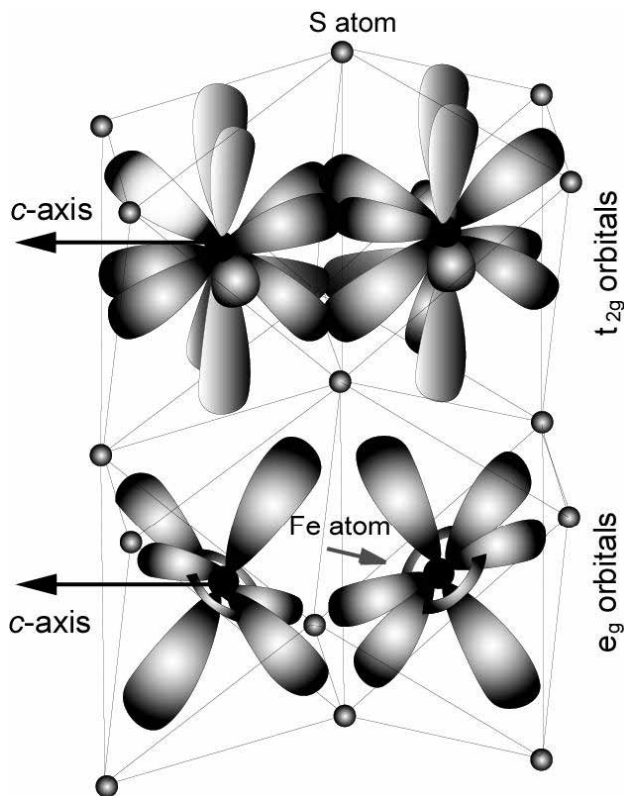


Figure 7. Ideal crystal structure of FeS with Fe 3d orbital  $e_g$  and  $t_{2g}$  orientation in  $[\text{FeS}_6]$  octahedrons [3].

The  $t_{2g}$  orbitals of iron do not contribute to Fe–S bonding in pyrrhotite and are predominantly non-bonding in character [42, 43]. According to Goodenough [114], Fe–Fe separation less than 3.0 Å in FeS leads to an overlapping of  $t_{2g}$  orbitals of adjacent Fe atoms. The overlapping produces  $\pi$ -bonded crystal orbitals along the  $c$  axis (figure 6) [3, 113]. The  $\pi$  (bonding) and  $\pi^*$  (anti-bonding) levels caused by adjacent Fe atoms are illustrated in figure 5 [3]. This overlapping of  $t_{2g}$  orbitals from neighbouring Fe atoms acts as conductive conduits, resulting in preferential electronic conductivity along  $c$ -axis. The  $e_g$  orbitals of two neighbouring Fe atoms are not overlapped compared to the slightly mixed  $t_{2g}$  orbitals (figure 7).

If there was no Fe–Fe  $\pi$ -bond produced, namely  $t_{2g}$  orbitals did not split into  $\pi$  (bonding), and  $\pi^*$  (anti-bonding) levels, the  $t_{2g}(\beta)$  is the highest occupied orbital forming the Fermi level. However, the formation of Fe–Fe  $\pi$ -bond splits  $t_{2g}(\beta)$  into  $\pi(\beta)$  and  $\pi^*(\beta)$  levels, makes the higher anti-bonding level,  $\pi^*(\beta)$ , fall into the conduction band. Therefore, the lower  $\pi(\beta)$  level is the highest occupied energy level and coincides with the Fermi level in pyrrhotite.

#### 4.3. Band diagram

Pyrrhotite consists of many  $[\text{FeS}_6]$  octahedrons, which form the crystal lattice of pyrrhotite. The energy levels are expected to be broadened into bands due to

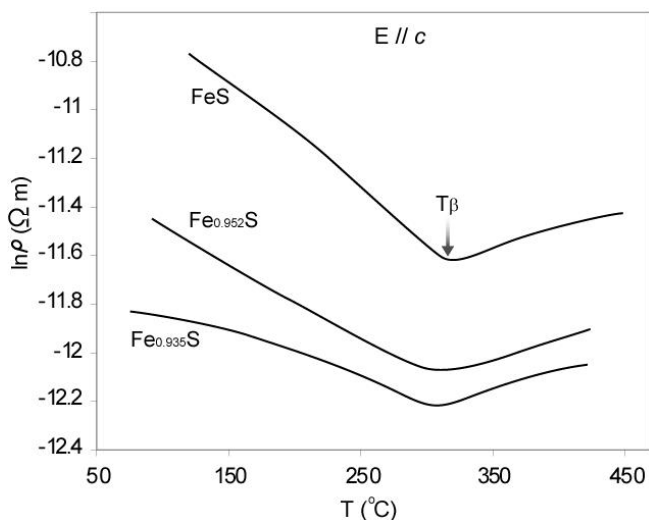


Figure 8. Temperature variation of the resistivity of pyrrhotite with different compositions [117].

the interactions among these octahedrons. The bandwidth depends on the extent of the overlapping with states of other atoms that surround each octahedron.

The major factors that affect the band structure of pyrrhotite are temperature and concentration of impurities. A conductivity transition occurs accompanied with this  $\beta$ -transition in pyrrhotite, from semiconducting behaviour to metallic behaviour [18, 115]. As shown in figure 8, below  $\beta$ -transition temperature all pyrrhotite samples (with different compositions) show negative temperature coefficients for resistivity ( $d\rho/dT < 0$ ), a property of semiconductors. Above  $315^\circ\text{C}$ , the positive slope of  $d\rho/dT$  indicates a clear metallic property.

It is not a mere coincidence that the conductivity transition (semiconducting  $\rightarrow$  metallic) and the magnetic transition (ferromagnetic/anti-ferromagnetic  $\rightarrow$  paramagnetic) occur at the same temperature ( $T_\beta$ ). Slater [116] and Sakkopoulos [117] proposed that in the temperature range  $T < T_\beta$ , the anti-ferromagnetically arranged magnetic moments accounts for the formation of semiconducting behaviour. For an anti-ferromagnetic system, the potential periodicity is twice the lattice spacing, caused by the anti-parallel orientation of magnetic moments. This doubly periodic potential splits the energy band into two. For example, the potential energy of an electron with  $+$  spin tends to exist in the atoms with spins in the  $+$ -direction, rather than in those with opposite spin [117].

In an electronic field, the vacancies in pyrrhotite act as charge carriers, forming impurity band (figure 9). It can be split into two sub-bands by the doubly periodic potential, leaving a narrow gap between them. The structure of band diagram for pyrrhotite evolves with increasing temperature. A broad S 3p valence band separated from the conduction band by  $0.8\text{ eV}$  composes the band structure. The one-third filled  $t_{2g}(\beta)$  band determines the level of Fermi energy, leaving an empty strip of  $0.2\text{ eV}$  from the top of the valence band. (Note:  $t_{2g}(\beta)$  band is different from the  $t_{2g}(\beta)$  energy level in energy level diagram. It is a collective effect of energy level broadening caused by lattice interaction [3, 113].) The impurity band

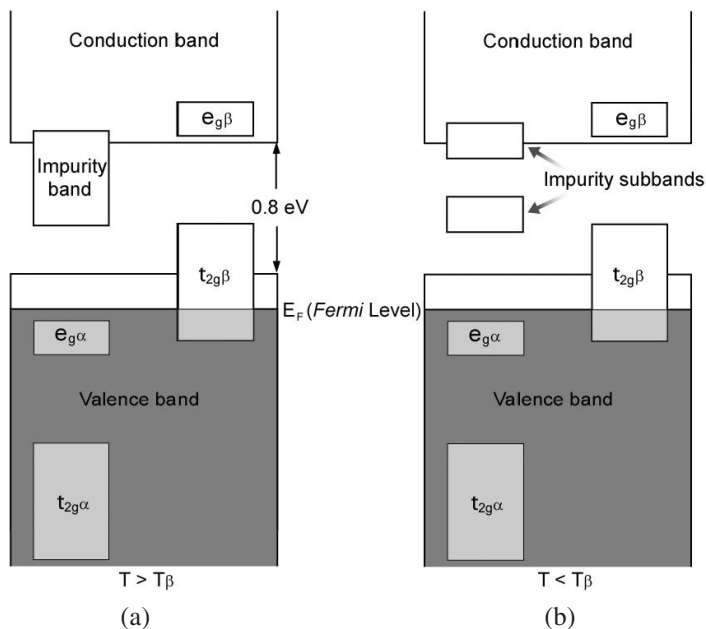


Figure 9. Energy band diagram for FeS. (a)  $T > T_\beta$ . The impurity band completely bridges the energy gap. (b)  $T < T_\beta$ . An energy gap produced by impurity sub-bands [90, 94].

locates near the bottom of the conduction band. For  $T > T_\beta$ , the impurity band and  $t_{2g}(\beta)$  band overlapped and the forbidden gap between conduction band and valence band is bridged, resulting in a metallic behaviour of pyrrhotite (figure 9a). For  $T < T_\beta$ , anti-ferromagnetically ordered moment splits the impurity band and leaves a narrow gap. This gap breaks the bridge formed by  $t_{2g}(\beta)$  band and impurity band, rendering a semiconducting behaviour of pyrrhotite (figure 9b).

#### 4.4. Vacancy effect

Apart from the effect on the formation of pyrrhotite superstructures, the presence of Fe vacancies gives rise to existence of iron hole states ( $\text{Fe}^{3+}$ ) in metal-deficient pyrrhotites. The existence of both  $\text{Fe}^{\text{II}}\text{-S}$  and  $\text{Fe}^{\text{III}}\text{-S}$  (hole state) in pyrrhotite has been confirmed by X-ray photoelectron spectroscopy (XPS) analysis [118]. The hole states are the results of charge compensation within the crystal structure and the number of hole states varies sympathetically with composition [42]. For the stoichiometric FeS, the charges of  $\text{Fe}^{2+}$  and  $\text{S}^{2-}$  are balanced; therefore there should be no hole state ( $\text{Fe}^{3+}$ ) detected in troilite. However, the experimental result from Skinner *et al.* [42] says otherwise. This can be explained with the aid of FeS–FeS<sub>2</sub> phase diagram. Increasing iron content to  $\text{Fe}/\text{S}=1$  causes the formation of 2C troilite where close Fe cluster is formed leading to an increase of metallic iron component.

Increased electron population within the conduction band arising from Fe 3d electron overlapping is confirmed by the XPS spectrum of troilite [42].

The vacancy also affects the conductivity of pyrrhotites. In metal-deficient pyrrhotites, electron conduction occurs preferentially along *c*-axis. In the stoichiometric pyrrhotite, FeS, however, the conductivity remains strong both along *c*-axis

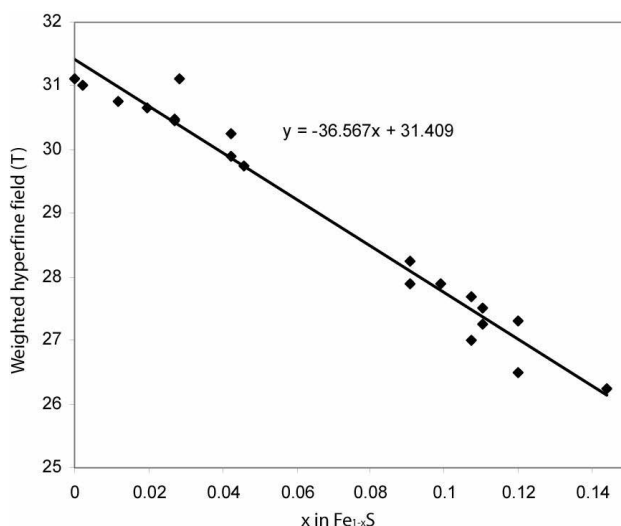


Figure 10. Variation of weighted hyperfine field,  $B_{\text{hf}}$ , with  $x$  in  $\text{Fe}_{1-x}\text{S}$  [36].

and in *ab*-plane, due to the shortening of Fe–Fe distance of the triangle Fe cluster in *ab*-plane [10, 42].

The existence of hole state ( $\text{Fe}^{3+}$ ) in FeS is expected to compensate the metallic iron in troilite. It is convenient to assign  $\text{Fe}^0$  to metallic iron in pyrrhotite when constructing the equation of charge balance, though it is not a true electron configuration according to orbital theory. The charge balance can be written as:  $\text{Fe}^0$  (metallic) +  $2\text{Fe}^{3+}$  (hole state)  $\rightarrow 3\text{Fe}^{2+}$ . This equation also applies to metal deficient pyrrhotites as to monoclinic pyrrhotite. However, with further increase in sulphur content, the pyrrhotite structure eventually breaks down to pyrite ( $\text{FeS}_2$ ), where  $\text{Fe}^{\text{II}}$  is almost the only state of iron. In the structure of pyrite,  $\text{Fe}^{\text{III}}$  is no longer needed for the charge compensation as it is in pyrrhotite.

Mössbauer spectroscopy is commonly used to study the vacancies ordering and coordination states of iron in pyrrhotite superstructures, accompanied with the conventional diffraction methods. In the NiAs structure, each iron atom is octahedrally coordinated to six sulphur atoms, but Mössbauer spectra of metal-deficient pyrrhotites demonstrated that sulphur is both five- and six-fold coordinated due to metal vacancies [42, 42, 119]. In troilite, the majority of iron lattice sites are filled and therefore we expect to observe increased six-fold coordinate sulphur at the expense of five-fold coordinate sulphur, as well as decreased  $\text{Fe}^{3+}$  atoms due to filling of iron vacancies. The Mössbauer spectra of monoclinic pyrrhotite are relatively narrower than that of the hexagonal *NC* phases, which is very broad and asymmetric due to the vacancy distribution and mixture of multiphases of *NC* structures [15, 36, 76, 120]. This broadening of the linewidths in the Mössbauer spectra indicated different short-range order around Fe sites, and a variation in the primitive unit cell axes in different pyrrhotite superstructures [36]. The atomic ratio Fe/S in  $\text{Fe}_{1-x}\text{S}$  can be correlated with the weighted hyperfine field,  $B_{\text{hf}}$ , which decreases when the at.% Fe decreases [15, 36, 66, 76, 121, 122], as shown in figure 10.

## 5. Magnetic structures

Pyrrhotite shows distinct magnetic anisotropy [123]. Along the direction parallel to the  $c$ -axis, the crystal is anti-ferromagnetic or ferrimagnetic (depending on vacancy concentration on cation layers parallel to the  $ab$ -plane), while perpendicular to the  $c$ -axis and within the same  $ab$ -plane the crystal is ferromagnetic (all spins orientate in the same direction) [100]. The magnetic transition sequence for the entire pyrrhotite group is illustrated in the schematic diagrams in figure 11 [11, 117, 124, 125]. The behaviour of magnetic moment ordering in more metal-deficient pyrrhotite is different from that in near stoichiometric FeS. More metal-deficient pyrrhotite ( $\text{Fe}_{1-x}\text{S}$ ,  $x > 0.05$ ) does not experience  $\alpha$ -transition, as does troilite. The  $\beta$ -transition, on the other hand, applies to all pyrrhotite composition and occurs at  $315^\circ\text{C}$ . At lower temperature ( $T < 315^\circ\text{C}$ ), magnetic moments are ferromagnetically orientated ( $\uparrow\uparrow\uparrow\uparrow$ ) in the same  $ab$ -plane, but anti-ferromagnetically coupled ( $\uparrow\downarrow\uparrow\downarrow$ ) with moments from adjacent  $ab$ -planes. Troilite shows the anti-ferromagnetic structure, in which net moments are neutralized to zero due to reversely orientated spin moments in adjacent  $ab$ -planes.

The ferrimagnetic structure of pyrrhotite ( $\text{Fe}_{1-x}\text{S}$ ,  $x > 0.05$ ) originates from an uneven distribution of vacancies in different  $ab$ -planes [126]. Since Fe is the carrier

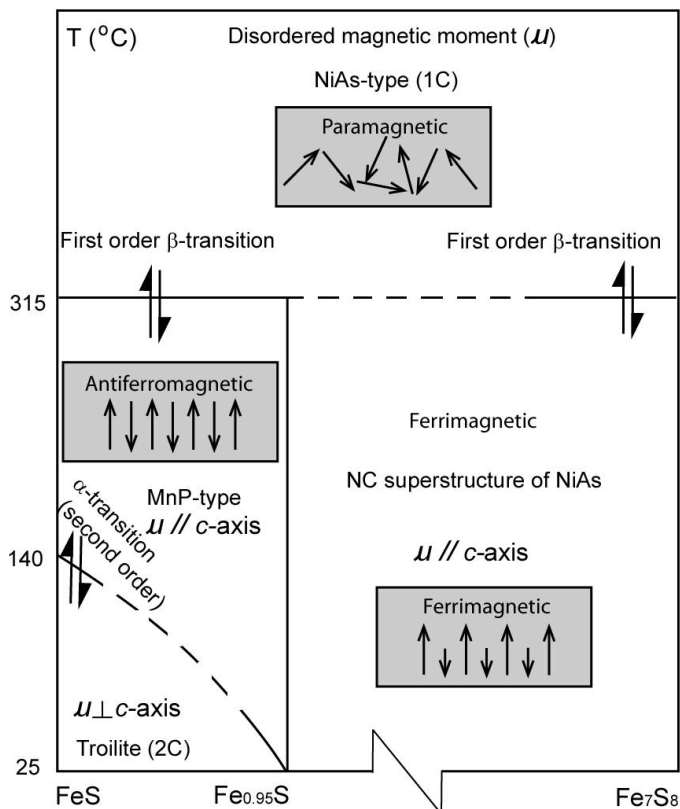


Figure 11. Schematic diagram of the magnetic transitions of pyrrhotite [11, 117, 124, 125].

of spin moment, the layers with cation vacancies display weaker magnetism than layers free of vacancy.

Over the whole composition range,  $\text{Fe}_{1-x}\text{S}$  ( $0 < x < 0.125$ ), pyrrhotite experience a so-called  $\beta$ -transition at  $T_\beta \approx 315^\circ\text{C}$ , in which former magnetically ordered phase changes to a paramagnetic phase. In the paramagnetic phase, the random orientation of magnetic moments results in zero net magnetic moment.

For  $\text{Fe}_7\text{S}_8$ , as the moment orientations in cation vacancy layer and fully occupied cation layer are anti-parallel, a non-zero net magnetic moment occurs as the result of uncompensated magnetic fields between neighbour *ab*-panes. For other pyrrhotite compositions, the magnetic field interaction between iron vacancy layer and vacancy free layer is more complicated. Ideally, the less metal-deficient the bulk pyrrhotite composition is, the weaker the net magnetic moment should be caused by uncompensated magnetic fields. However, the true relationship between pyrrhotite composition and the net magnetic moment is not restrictively linear; the relationship follows a damping periodic pattern as shown in figure 12.

Some indirect evidence from thermal magnetization experiments provided by Li and Franzen [49] have demonstrated the existence of this periodic damping relationship. In order to explain this phenomenon, it is necessary to determine the magnetic structure consistent with a given *NC* superstructure. First of all, consider the stacking sequences in 4C, 5C, 6C, and 11C in figure 13 [73, 127, 128]. For 4C structure, all the vacancy layers (ABCD) orientate in the same direction ( $\uparrow$ , up in figure 13), all the vacancy free layers (F) also orientate in the same direction ( $\downarrow$ , down in figure 13) but anti-parallel to the vacancy layers [52, 53, 67, 73, 127, 128]. This arrangement of magnetic moment produces the maximum ferrimagnetic behaviour. For 5C, 6C, and 11C structures, however, both the vacancy layers and full layers can orientate either way ( $\uparrow$ , up and  $\downarrow$ , down in figure 13). This arrangement counterbalances the magnetic moment from each direction, resulting in anti-ferromagnetism. Therefore, the minima of the net magnetic moment occur at  $\text{Fe}_9\text{S}_{10}$  (5C),  $\text{Fe}_{11}\text{S}_{12}$  (6C), and  $\text{Fe}_{10}\text{S}_{11}$  (11C) in figure 12.

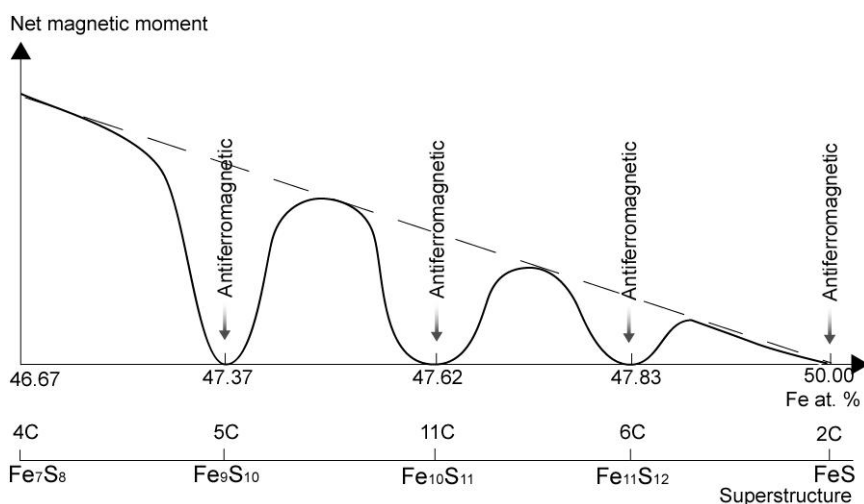


Figure 12. Periodical pattern of the relationship between pyrrhotite composition and net magnetic moment.

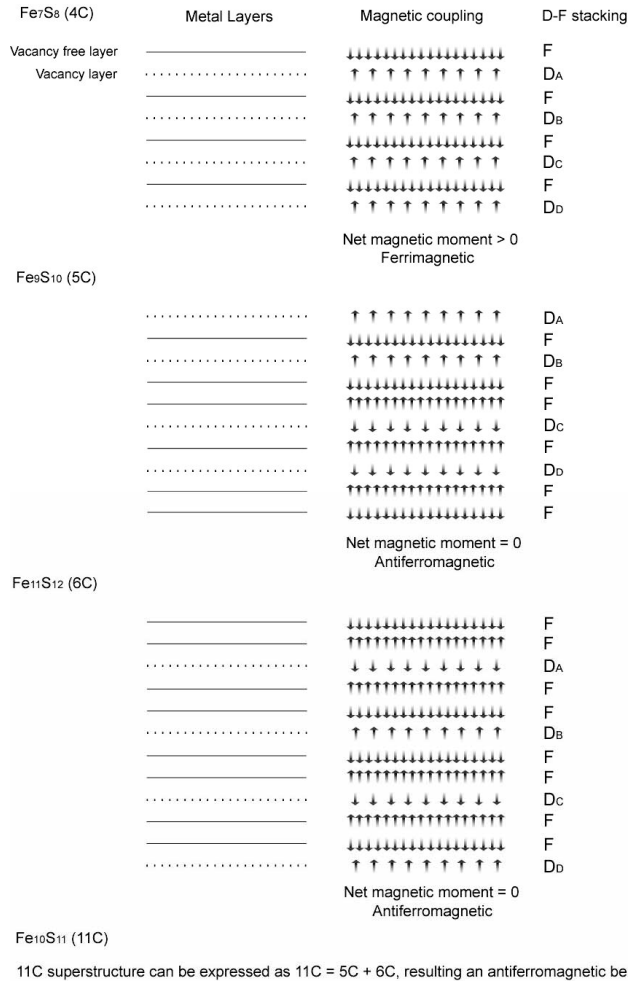


Figure 13. Stacking sequence of the metal vacancy layer and vacancy free layer for 4C, 5C, 6C, and 11C structure [52, 53, 67, 73, 127, 128].

6. Concluding remarks

Pyrrhotite group minerals are abundant in nature, involved in myriad mineralogical and metallurgical fields. However, they are extremely complicated from both crystallographic and chemical standpoints due to their non-stoichiometric nature, various polymorphs, and variable magnetic and electronic properties. Better understanding of the mineral chemistry and physics of these minerals benefits many industrial and scientific areas. There are many compositional and crystallographic variations of pyrrhotite minerals that merit consideration from researchers with different backgrounds. This article summarized works of numerous researchers to illustrate the phase relations between various polymorphs of pyrrhotite group minerals. However, some phase transitions in certain composition/temperature ranges still remain unclear. For example, the  $\alpha$ - and  $\beta$ -transition curves of pyrrhotite have never been established. These all need further studies.

## Acknowledgements

Haipeng Wang would like to thank the Australian Education, Science, and Training Department for the APA award, which has allowed this work to be carried out.

## References

- [1] R.G. Arnold, *Am. Mineral.* **51** 1221 (1966).
- [2] R.H. Carpenter and G.A. Desborough, *Am. Mineral.* **49** 1350 (1964).
- [3] H.W. Nesbitt, A.G. Schaufuss, G.M. Bancroft and R. Szargan, *Phys. Chem. Minerals* **29** 72 (2002).
- [4] D.J. Vaughan and J.R. Craig, *Mineral Chemistry of Metal Sulphides* (Cambridge University Press, Cambridge, 1978).
- [5] H. Wang, A. Pring, Y. Ngothai and B. O'Neill, *Thermochim. Acta* **427** 13 (2005).
- [6] J.G. Dunn and V.L. Howes, *Thermochim. Acta* **282/283** 305 (1996).
- [7] A. Lu, J. Chen, J. Shi, X. Lu and J. Tang, *Chinese Science Bulletin* **45** 1614 (2000).
- [8] S.A. Kissin and S.D. Scott, *Econ. Geol.* **77** 1739 (1982).
- [9] E.F. Bertaut, *Comptes Rendus* **234** 1295 (1952).
- [10] H.T. Evans, *Science* **167** 621 (1970).
- [11] F. Li and H.F. Franzen, *J. Alloys Compd.* **238** 73 (1996).
- [12] J.C. Ward, *Rev. Pure Appl. Chem.* **20** 175 (1970).
- [13] J.M.D. Coey, H. Roux-Buisson and R. Brusetti, *J. Phys.* **C4** 1 (1976).
- [14] J.E. Thomas, W.M. Skinner and R.St.C. Smart, *Geochim. Cosmochim. Acta* **67** 831 (2003).
- [15] O. Kruse, *Am. Mineral.* **75**, 755 (1990).
- [16] V.H. Haraldsen, *Z. Anorg. Allg. Chem.* **26** 195 (1941).
- [17] J.T. Sparks, W. Mead and T. Komoto, *J. Phys. Soc. Japan Suppl.* **17B-1** 249 (1962).
- [18] E. Hirahara and M. Murakami, *J. Phys. Chem. Solids* **7** 281 (1958).
- [19] J.T. Sparks and T.O. Komoto, *Rev. Mod. Phys.* **40** 40 (1968).
- [20] T.B. Massalski (Editor), *Binary Alloy Phase Diagram*, 2nd Edn (AMS International, New York, 1990).
- [21] G.A. Desborough and R.H. Carpenter, *Econ. Geol.* **60** 1431 (1965).
- [22] W.G. Moffatt (Editor), *The Handbook of Binary Phase Diagrams*, Vol. 3 (General Electric, New York, 1984).
- [23] W. Treitschke and G. Tammann, *Z. Anorg. Allg. Chem.* **49** 320 (1906).
- [24] E.T. Allan, J.L. Crenshaw, J. Johnson and E.S. Larsen, *Z. Anorg. Allg. Chem.* **76** 201 (1912).
- [25] R. Juza and W. Blitz, *Z. Anorg. Allg. Chem.* **205** 273 (1932).
- [26] S. Hägg, *Zeit. Physik. Chem.* **B22** 444 (1933).
- [27] H. Haraldsen, *Z. Anorg. Allg. Chem.* **231** 78 (1937).
- [28] E.F. Bertaut, *Bull. Soc. Fr. Miner. Cristallogr.* **79** 276 (1956).
- [29] A. Putnis, *Science* **186** 439 (1970).
- [30] A.F. Andersen and P. Torbo, *Acta Chem. Scand.* **21** 2841 (1967).
- [31] J.T. Sparks, W. Mead, A.J. Kirschbaum and W. Marshall, *J. App. Phys.* **31**(5) (Suppl.) 699 (1960).
- [32] M.E. Fleet and N. MacRae, *Can. Mineral.* **9** 699 (1969).
- [33] R.G. Arnold, *Economic Geology* **64** 405 (1969).
- [34] H.E. King and C.T. Prewitt, *Acta Crystallogr.* **B38** 1877 (1982).
- [35] O. Kruse, *Am. Mineral.* **77** 391 (1992).
- [36] J.W.A. Kondoro, *J. Alloys Compd.* **289** 36 (1999).
- [37] L.M. Levinson and D. Treves, *J. Phys. Chem. Solids* **29** 2227 (1968).
- [38] J. Flahaut, Transition metal chalcogenides, in *MTP International Review of Science, Solid State Chemistry, Inorganic Chemistry Series One*, edited by L.E.J. Roberts, Vol. 10 (Butterworths University Park Press, London, 1972), pp. 189–240.
- [39] M. Corlett, *Zeitschrift für Kristallographie* **126** 124 (1968).

- [40] W. O'Reilly, V. Hoffmann, A.C. Chouker, H.C. Soffel and A. Menyeh, *Geophys. J. Int.* **142** 669 (2000).
- [41] M. Tokonami, K. Nishihiguchi and N. Morimoto, *Am. Mineral.* **57** 1066 (1972).
- [42] W.M. Skinner, H.W. Nesbitt and A.R. Pratt, *Ceochim. Cosmochim. Acta* **68** 2259 (2004).
- [43] J.A. Tossell, *J. Chem. Phys.* **66** 5712 (1977).
- [44] D.J. Vaughan and M.S. Ridout, *Solid State Commun.* **8** 2165 (1970).
- [45] L. Néel, *Rev. Mod. Phys.* **25** 58 (1953).
- [46] A.V. Powell, P. Vaquero, K.S. Knight, L.C. Chapon and R.D. Sánchez, *Phys. Rev.* **B70** 1 (2004).
- [47] A.H. Clark, *Trans. Inst. Mining Met.* **B232** 75 (1966).
- [48] G. Kullerud, B.R. Deo, P.R. Buseck and P.F. Troften, *Carnegie Inst. Year Book* **62** 210 (1962).
- [49] F. Li and H.F. Franzen, *J. Solid-state Chem.* **126** 108 (1996).
- [50] M.E. Fleet, *Acta Crystallogr.* **B27** 1864 (1971).
- [51] A. Okazaki and K. Hirakawa, *J. Phys. Soc. Japan* **11** 390 (1956).
- [52] F. Keller-Besrest, G. Collin and R. Comès, *Acta Crystallogr.* **B38** 296 (1982).
- [53] F. Li, H.F. Franzen and M. Krame, *J. Solid-state Chem.* **124** 246 (1996).
- [54] M. Tokomi, K. Nishiguchi and N. Morimoto, *Am. Mineral.* **57** 1066 (1972).
- [55] H. Nakazawa, M. Tokonami and N. Morimoto, *Acta Crystallogr.* **B35** 722 (1979).
- [56] T. Ericsson, Ö. Amcoff and P. Nordblad, *Eur. J. Mineral.* **9** 1131 (1997).
- [57] F.K. Logtering, *Philips Rev. Rep.* **12** 190 (1956).
- [58] K. Hirakawa, *J. Phys. Soc. Jpn.* **12** 929 (1957).
- [59] M. Kawaminami and A. Okazaki, *J. Phys. Soc. Jpn.* **29** 649 (1970).
- [60] E.F. Bertaut, *Acta Crystallogr.* **6** 557 (1953) (in French).
- [61] L.A. Marusak and L.L. Tongson, *J. Appl. Phys.* **50** 4350 (1979).
- [62] N. Morimoto, *Memoirs of the Institute of Science and Industrial Research*, Vol. 36 (Osaka University, Osaka, 1978), p. 45.
- [63] H. Nakazawa and N. Morimoto, *Am. Mineral.* **60** 359 (1975).
- [64] K. Igaki, M. Sata and T. Shinohara, *Trans. Jpn. Inst. Metals* **22** 627 (1981).
- [65] K. Igaki, M. Sata and T. Shinohara, *Trans. Jpn. Inst. Metals* **23** 221 (1982).
- [66] K. Ono, A. Ito and E. Hirahara, *J. Phys. Soc. Jpn* **17** 1615 (1962).
- [67] L. Pierce and P.R. Buseck, *Science* **186** 1209 (1974).
- [68] H. Nakazawa and N. Morimoto, *Japanese Acad. Proc.* **46** 678 (1970).
- [69] H. Nakazawa and N. Morimoto, *Mater. Res. Bull.* **6** 345 (1971).
- [70] N. Morimoto, A. Gyobu, K. Tsukuma and K. Koto, *Econ. Geol.* **70** 824 (1975).
- [71] N. Morimoto, A. Gyobu, K. Tsukuma and K. Koto, *Am. Mineral.* **60** 240 (1975).
- [72] F. Grønbold and S. Stølen, *J. Chem. Thermodyn.* **24** 913 (1992).
- [73] K. Koto, N. Morimoto and A. Gyobu, *Acta Crystallogr.* **B31** 2759 (1975).
- [74] N. Morimoto, *Rec. Prog. Nat. Sci. Jpn.* **3** 183 (1978).
- [75] L.F. Power and H.A. Fine, *Miner. Sci. Eng.* **8** 107 (1976).
- [76] N.S. Ovanesyan, G. Trukhtanov, Y.G. Odinets and G.V. Novikov, *Sov. Phys. J. Exp. Theor. Phys.* **33** 1193 (1971).
- [77] A. Putnis and J.D.C. McConnell, *Principles of Mineral Behaviour* (Blackwells, Oxford, 1980), p. 257.
- [78] A.J. Naldrett and G. Kullerud, *J. Petrol.* **8** 453 (1967).
- [79] S. Chikazumi, *Physics of Magnetism* (John Wiley & Sons, New York, 1964), p. 554.
- [80] L.A. Taylor, *Carnegie Inst. Washington Year Book* **68** 259 (1970).
- [81] L. Kübler, *Phys. Chem. Minerals* **8** 8 (1982).
- [82] A. Genkin, *Mineralium Deposita* **6** 348 (1971).
- [83] R.G. Arnold, *Econ. Geol.* **57** 72 (1962).
- [84] R.A. Yund and H.T. Hall, *Econ. Geol.* **64** 420 (1969).
- [85] L.S. Darken, *Trans. Met. Soc. A.I.M.E.* **239** 80 (1967).
- [86] S.A. Kissin, Phase relations in a portion of the Fe-S system. PhD thesis, University Toronto (1974).
- [87] R.G. Arnold, *Can Mineral.* **9** 31 (1967).
- [88] S.D. Scott, *Fortschr. Mineralogie* **52** 185 (1975).
- [89] S.D. Scott and H.L. Barnes, *Econ. Geol.* **66** 653 (1971).
- [90] P. Toulmin and P.B. Barton, *Geochim. Cosmochim. Acta* **28** 641 (1964).

- [91] H.L. Barnes, Investigation in hydrothermal sulfide system in *Research Techniques for High Pressure and High Temperature*, edited by G.C. Ulmer (Springer-Verlag, New York, 1971), pp. 317–355.
- [92] L.A Taylor, Carnegie Inst. Washington Year Book **69** 325 (1971).
- [93] L. Kübler and B. Lundqvist, *Lithos* **12** 241 (1979).
- [94] L.A. Taylor and H.K. Mao, *Science* **170** 850 (1970).
- [95] A. Sugaki, H. Shima, A. Kitakaze and M. Fukuoka, Tohoku Univ. Sci. Rept., series 3 **13** 147 (1977).
- [96] A. Sugaki, H. Shima, A. Kitakaze and M. Fukuoka, *J. Miner. Soc. Jpn.* **11** 63 (1974).
- [97] A. Sugaki, H. Shima, A. Kitakaze and M. Fukuoka, Tohoku Univ. Sci. Rept., series 3 **13** 165 (1977).
- [98] G. Kullerud and H.S. Yoder, *Econ. Geol.* **54** 533 (1959).
- [99] S.D. Scott and S.A. Kissin, *Econ. Geol.* **68** 475 (1973).
- [100] A.H. Craig, *Inst. Mining Metallurgy Trans.* **75B** 232 (1966).
- [101] K. Hayas and T. Mariko, *Geol. Soc. Jpn. J.* **67** 1 (1961).
- [102] E. Izawa and H. Mukaiyama, Thermally metamorphosed sulfide mineral deposits, paper presented at the 24th Japanese International Geology Congress, Montreal, section 4 (1972), pp. 455–462.
- [103] N. Morimoto and H. Nakazawa, *Science* **161** 577 (1968).
- [104] H. Mukaiyama and E. Izawa, *Mining. Inst. Kyushu J.* **34** 194 (1966).
- [105] A. Vorma, *Geol. Soc. Finland Bull.* **42** 3 (1970).
- [106] C.J. Ballhausen, *Introduction to Ligand Field Theory* (McGraw-Hill, New York, 1962), pp. 108–110.
- [107] H.A. Jahn and E. Teller, *Proc. Royal Soc.* **A161** 220 (1937).
- [108] H.A. Jahn, *Proc Royal Soc.* **A164** 117 (1938).
- [109] L.E. Orgel, *An Introduction to Transition-Metal Chemistry*, 2nd Edn (Wiley, New York, 1966), pp. 57–61.
- [110] J.D. Dunitz and L.E. Orgel, *Adv. Inorg. Chem. Radiochem.* **2** 1 (1960).
- [111] C.R. Ollis, *J. Am. Chem. Soc.* **93** 547 (1971).
- [112] F.A. Cotton, *Chemical Applications of Group Theory*, 2nd Edn (Wiley, New York, 1970), p. 230.
- [113] S. Sakkopoulos, E. Vitoratos and T. Argyreas, *J. Phys. Chem. Solids* **45** 923 (1984).
- [114] J. Goodenough, *J. Appl. Phys. Suppl.* **33** 1197 (1962).
- [115] J.L. Horwood, M.G. Townsend and A.H. Webster, *J. Solid State Chem.* **17** 35 (1976).
- [116] J.C. Slater, *Phys. Rev.* **82** 538 (1951).
- [117] S. Sakkopoulos, *J. Appl. Phys.* **59** 3540 (1986).
- [118] A.R. Pratt, I.J. Muir and H.W. Nesbitt, *Geochim. Cosmochim. Acta* **58** 827 (1994).
- [119] E.F. Bertaut, *Bull. Soc. Fr. Mineral. Crist.* **79** 276 (1953).
- [120] L.A. Marusak and L.N. Mulay, *J. Appl. Phys.* **50** 1865 (1979).
- [121] C. Jeandey, J.L. Oddou, J.L. Mattei and G. Fillion, *Solid State Commun.* **78** 195 (1991).
- [122] W. Keune and A.S. Camara, *Phys. Status Solidi* **27a** 181 (1975).
- [123] A. Theodossiou, *Phys. Rev.* **137** 1321 (1965).
- [124] W.G. Marshall, R.J. Nelmes, J.S. Loveday, S. Klotz, J.M. Besson, G. Hamel and J.B. Parise, *Phys. Rev.* **B61** 11201 (2000).
- [125] C. Kittel, *Introduction to Solid State Physics*, 6th Edn (John Wiley & Sons, New York, 1986).
- [126] F. Grønvold and S. Støen, *J. Chem. Thermodyn.* **23** 261 (1991).
- [127] K. Koto and M. Kitamura, *Acta Crystallogr.* **A37** 301 (1981).
- [128] I. Dodony and M. Posfai, *Eur. J. Mineral.* **2** 529 (1990).